ACS Catalysis

Research Article

Cite This: ACS Catal. 2018, 8, 11042−11053

pubs.acs.org/acscatalysis

# Deconvoluting the Competing Effects of Zeolite Framework Topology and Diffusion Path Length on Methanol to Hydrocarbons Reaction

Yufeng Shen,[†] Thuy T. Le,[†] Donglong Fu,[‡] Joel E. Schmidt,[‡] Matthias Filez,[‡] Bert M. Weckhuysen,*[,‡] and Jeffrey D. Rimer*[,†]

[†]Department of Chemical and Biomolecular Engineering, University of Houston, 4726 Calhoun Road, Houston, Texas 77204, United States

[‡]Inorganic Chemistry and Catalysis Group, Debye Institute for Nanomaterials Science, Utrecht University, Universiteitsweg 99, 3584 CG Utrecht, The Netherlands

Supporting Information

**ABSTRACT:** Micropore topology and crystal size are two independently adjustable properties that govern the internal mass transport limitations of zeolite catalysts. Deciphering the relative impact of each factor on catalyst performance is often nontrivial owing to the inability to synthesize zeolites with predetermined physicochemical properties. In this study, a series of ZSM-11 (MEL) and ZSM-5 (MFI) catalysts of equivalent acidity, but differing pore architecture, are prepared with well-defined crystal sizes to elucidate the effects of diffusion path length versus topology on catalyst lifetime and selectivity. For these studies, we selected the methanol to hydrocarbons (MTH) reaction to assess the impact of design variables on the hydrocarbon pool (HCP) mechanism. Operando UV−vis microspectroscopy is used to investigate the evolution of active HCP species and heavier aromatic coking species during the transient start up period over both catalysts. Our findings reveal that slight variations in framework topology between MEL and MFI zeolites lead to marked differences in their catalytic performance as well as the evolutionary behavior of HCP species within the zeolite pores. We report that the diffusion limitations imposed by the tortuous channels in ZSM-5 catalysts are analogous to increasing the channel length in ZSM-11 catalysts via larger crystal sizes. Notably, we observe similar (albeit slightly offset) trends in MTH selectivity and HCP speciation for both zeolite framework types; however, differences in pore topology and catalyst size exact different effects on the evolution of intracrystalline hydrocarbon species. Collectively, these findings provide evidence that ZSM-11 is an effective medium-sized pore zeolite catalyst for reactions encumbered by rapid coking that often elicits premature deactivation.

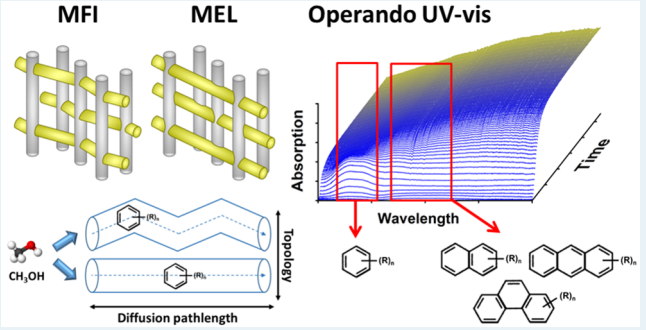


**KEYWORDS:** *ZSM-11, ZSM-5, zeolite, aromatics, $C_1$ chemistry*

## 1. INTRODUCTION

Methanol to hydrocarbons (MTH) is an increasingly utilized industrial process as the world economy gradually trends away from crude oil dependency with concomitant increases in the demand for gasoline and petroleum derived products.[1,2] MTH is a central step in many fuel and olefin production processes that utilize alternative carbon sources, such as natural gas, biomass, and coal.[3] Subsets of the general MTH process include methanol to gasoline (MTG), methanol to olefins (MTO), and other variations of the aforementioned reactions.[4] Zeolite catalysts play an important role in directing and improving these industrial processes, yet only zeotype SAPO-34 (CHA) and zeolite ZSM-5 (MFI) are reported to be used commercially.[5−7] A ubiquitous problem of these and other catalysts in hydrocarbon processing reactions is deactivation due to coking.[8] To this end, numerous studies have focused on elucidating structure-deactivation relationships for zeolite catalysts in MTH reactions.[9−14] The judicious selection of framework topology can minimize catalyst deactivation, while also impacting MTH reaction selectivity and catalyst activity.[15−17] Prior studies often compare zeolite frameworks with significant differences in pore size, cage/intersection size, and/or pore dimensionality and connectivity between samples; however, direct comparison between two very similar zeolite frameworks can be challenging given the difficulty of controlling additional physicochemical properties that influence catalyst performance, such as crystal size and morphology as well as acid site density and distribution. As such, when comparing two or more different zeolite frameworks, it is imperative to synthesize catalysts with fixed properties while allowing for only a single variable to be systematically altered.

Received: June 11, 2018
Revised: September 13, 2018
Published: September 19, 2018






DOI: 10.1021/acscatal.8b02274
ACS Catal. 2018, 8, 11042−11053

In this study, we compare the catalytic performance of two zeolite topologies: MFI (ZSM-5) and MEL (ZSM-11). As illustrated in Figure 1, both framework types exhibit almost identical

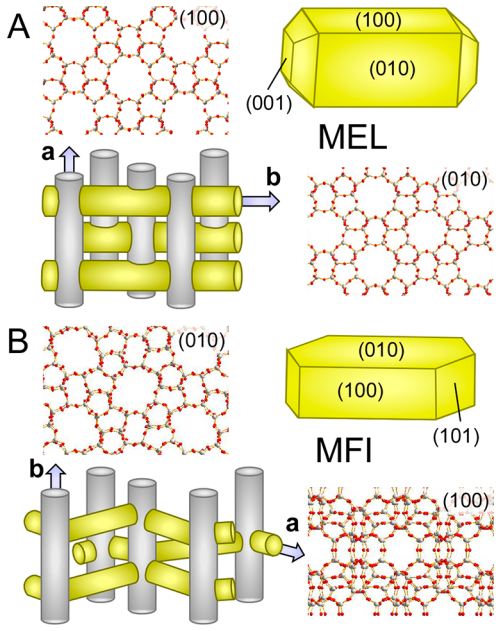


**Figure 1.** Crystal structure, micropore topology, and the typical morphology of (A) MFI (ZSM-11) and (B) MEL (ZSM-5) framework types. Arrows indicate channels aligned in the *a*- and *b*-directions. The *a*−*b* micropore dimensions (in units of Å) are (5.3 × 5.4):(5.3 × 5.4) for MEL and (5.1 × 5.5):(5.3 × 5.6) for MFI.

pore networks with two notable exceptions: (1) MFI has both straight and sinusoidal microporous channels, whereas all the channels in MEL are straight; (2) all channel intersections in MFI are identical, while MEL is comprised of two pore intersections (one having approximately the same size as MFI and the other with ca. 30% larger size).[15,18] Straight channels in zeolites are generally more efficient for molecular diffusion and can thus impact the rates of secondary reactions and coking (i.e., catalyst deactivation). Larger volumes at the intersection of pores can accommodate larger molecules in the hydrocarbon pool (HCP) of MTH reactions, which alters the selectivity toward heavier aromatic compounds. There are several studies comparing ZSM-5 and ZSM-11 in various reactions,[19−22] including MTH;[15,22,23] however, few comparisons are made among samples of equivalent physicochemical properties (e.g., crystal size, morphology, and composition) to allow for side-by-side analyses.

The effect of zeolite crystal size in MTH reactions has been studied for MFI[24,25] and CHA,[26−28] while similar investigations of MEL[29] are relatively scarce. The general conclusion in these studies is that smaller crystal size enhances the time on stream (TOS) lifetime of catalysts, consistent with a concomitant reduction in the internal mass transport limitations. Ryoo and co-workers successfully synthesized 2-dimensional MFI nanosheets with [010] dimensions of ca. 2 nm (i.e., on the order of a unit cell) and showed by comparison with a conventional ZSM-5 catalyst that the former dramatically extended the catalyst lifetime.[30] Bleken et al.[15] compared the lifetime of ZSM-5 and ZSM-11 catalysts in MTH reactions, showing an approximate 3-fold increase in lifetime for ZSM-11; however, catalyst samples used in their study exhibited disparate crystal sizes, rendering the direct comparison of diffusion path length complex. Bhan and co-workers[24] provided a systematic study of ZSM-5 crystal size effects in MTH reactions, showing that the selectivity toward light olefins (notably ethene) decreases with decreasing catalyst size, leading to an associated increase in the selectivity toward heavier aliphatic and aromatic products. In their study, Bhan and co-workers[24] attributed the effect of crystal size to differences in the length of pores across the zeolite particle, which impacts the internal diffusion of product molecules and the concentration of the HCP species. One of the challenges encountered during the preparation of catalysts with large variations in crystal size is the unintended alteration of other properties, such as the Si/Al ratio, which can have a notable impact on catalyst performance.[31] Indeed, it can be challenging to simultaneously tailor a single physicochemical property of the catalyst during synthesis, while holding all other properties constant, in order to properly evaluate structure-performance relationships.

Herein, we present a systematic study where the mass transport limitations imposed by the zeolite pore topology and diffusion path length are independently evaluated on the basis of their impact on the MTH reaction. ZSM-5 and ZSM-11 catalysts were synthesized with nearly identical crystal size and Si/Al ratio in order to demonstrate how slight differences in framework topology can impact reaction performance. Operando UV−vis spectroscopy of these catalysts reveals the evolution of both active intermediate hydrocarbon species and heavy coking species. On the basis of the time-resolved analysis of HCP products and intermediates, we are able to rationalize the underlying differences in selectivity between ZSM-5 and ZSM-11 catalysts. The effect of diffusion path length is investigated in detail using a set of ZSM-11 catalysts with varying crystal size. From these studies, we are able to formulate more detailed conclusions about the impact of mass transport limitations on HCP speciation and catalyst performance in MTH reactions.

## 2. EXPERIMENTAL SECTION

**2.1. Materials.** Zeolite synthesis was performed with the following reagents: tetraethyl orthosilicate (TEOS, 98%, Sigma-Aldrich), sodium aluminate (technical grade, Alfa Aesar), sodium hydroxide (>98%, Sigma-Aldrich), tetrabutylammonium hydroxide (TBAOH, 40%, Sigma-Aldrich), and tetrapropylammonium hydroxide (TPAOH, 40%, Alfa Aesar). All reagents were used as received without further purification. Deionized (DI) water, used in all experiments, was purified with an Aqua Solutions Type I RODI filtration system (18.2 MΩ). The 1.0 M ammonium nitrate solution used in ion exchange was made from ammonium nitrate salt ($NH_3NO_4$, ACS reagent, ≥98%, Sigma-Aldrich) and DI water. For reaction testing, the zeolite catalysts were pelletized and sieved (40−60 mesh size), and 36.9 mg of sieved catalyst pellets was diluted with 113.1 mg of silica gel (Davisol grade 636, 35−60 mesh particle size, Sigma-Aldrich).

**2.2. Catalyst Preparation.** For the synthesis of ZSM-11 zeolite, TBAOH was used as the organic structure-directing agent (OSDA). In a typical synthesis, 0.132 g of sodium aluminate was added to a mixture of 0.470 g of NaOH solution (43 mg/g of solution) and 1.24 g of DI $H_2O$. To this solution was added 3.55 g of TBAOH, followed by the silica source, TEOS (5.81 g). The resulting mixture was stirred at room temperature in a sealed bottle for 2 h to allow for the hydrolysis of


DOI: 10.1021/acscatal.8b02274
ACS Catal. 2018, 8, 11042−11053

TEOS. The molar compositions of synthesis mixtures listed in Table 1 were varied to produce catalyst sizes of 150, 300, and 750 nm. The procedure for ZSM-5 zeolite synthesis was identical to that of ZSM-11, with the exception that TPAOH was used as the OSDA. Herein, we use the nomenclature MEL-A or MFI-A to refer to catalyst samples, where $A$ = average crystal size (in units of nanometers, as confirmed by electron microscopy).

**Table 1. Synthesis Conditions for Catalyst Preparation**

| | synthesis molar composition | | | | | | |
|---|---|---|---|---|---|---|---|
| sample | TBAOH | $Na_2O$ | $SiO_2$ | $Al_2O_3$ | $H_2O$ | $T$ (°C) | time (days) |
| MEL-150 | 20 | 4 | 100 | 2.5 | 600 | 170 | 3 |
| MEL-300 | 20 | 4 | 100 | 2.5 | 1000 | 170 | 3 |
| MEL-750 | 20 | 4 | 100 | 2.5 | 2000 | 160 | 1 |
| MFI-300 | 20 | 4 | 100 | 2.5 | 2500 | 170 | 2 |

Each zeolite mixture prepared in Table 1 was placed in a 23 mL Teflon liner within a metal autoclave (Parr Instruments) that was sealed and heated in a Thermo Fisher Precision oven at temperatures $T$ = 160 or 170 °C and autogenous pressures. The autoclave was removed from the oven after a period of time (1 to 3 days) and was quenched in water to room temperature. The crystalline product (Na-ZSM-11 or Na-ZSM-5) was removed from the mother liquor by six cycles of centrifugation and washes with DI water, using a Beckman Coulter Avanti J-E centrifuge at 5 °C and 13 000 rpm for 10−45 min per cycle. Samples for catalysis were calcined in a Thermo Fisher Lindberg Blue furnace under constant flow of dried air (Matheson Tri-Gas) at 550 °C for 5 h with a temperature ramping/cooling rate of 1 °C/min. These samples were converted to an acid form (Brønsted acids) by ion exchange wherein calcined zeolite was mixed with 1.0 M ammonium nitrate solution to obtain a 2 wt % suspension. This mixture was heated to 80 °C for 2 h to allow the exchange of $Na^+$ with $NH_4^+$. This process was performed three times with centrifugation/washing between each ion exchange cycle. The final $NH_4$-zeolite samples were washed thrice with DI water before they were calcined once again with the same conditions stated above to generate H-form zeolites.

**2.3. Physicochemical Characterization of Zeolites.** H-form zeolites were characterized by powder X-ray diffraction (XRD) using a Rigaku SmartLab Diffractometer with Cu K$\alpha$ radiation to verify the crystalline structure (MEL and/or MFI). Powder XRD patterns were compared to simulated patterns of each framework type provided by the International Zeolite Association Structure Database.[32] The average crystal size was measured from scanning electron microscopy (SEM) images taken on a FEI 235 dual-beam (focused ion-beam) instrument. Elemental analysis of H-form zeolites was performed to confirm completion of ion exchange and to quantify the molar Si/Al ratio by energy dispersive spectroscopy (EDS) analysis using a JEOL SM-31010/METEK EDAX system at 15 kV and 15 mm working distance. To confirm the uniform Al distribution in the crystal, surface elemental analysis was performed with X-ray photoelectron spectroscopy (XPS) using a PHI 5800 ESCA (Physical Electronics) system, which is equipped with a standard achromatic Al K$\alpha$ X-ray source (1486.6 eV) operating at 300 W (15 kV and 20 mA) and a concentric hemispherical analyzer. Since zeolites are insulating materials, the equipment neutralizer component was utilized to prevent charging effects. All data was collected at a 45° takeoff angle, and collected spectra were analyzed using the MultiPak program. Textural analysis of H-form samples was performed to obtain the BET surface area using $N_2$ adsorption with a Micromeritics ASAP 2020 instrument, and microporous volume was determined from the t-plot method. Temperature-programmed desorption of ammonia ($NH_3$-TPD) was performed on a Micromeritics Autochem II 2920 equipped with a TCD detector. Prior to TPD, ca. 100 mg of catalyst was first outgassed in He for 1 h at 600 °C with a heating ramp of 10 °C/min. Ammonia was adsorbed at 100 °C until saturated, followed by flushing with He for 120 min at 100 °C. The ammonia desorption was monitored using the TCD detector until 600 °C with a ramp of 10 °C/min, using a flow of 25 mL/min. The relevant diffusion time scales for 2,2-dimethylbutane (22DMB; $R^2/D$) were measured by the Bhan Group (U. Minnesota) from the transient uptake of 22DMB using Micromeritics ASAP 2020 surface area and porosity analyzer equipped with a vapor option using the rate of adsorption software. Catalyst samples (~25 mg) were outgassed at 300 °C (0.017 °C/s) for 2 h and then cooled to analysis temperatures (80 °C). The samples were fully evacuated (<1 mTorr) before a known amount of sorbate was introduced (~5 Torr) and allowed to reach equilibrium. Measured transient sorption curves are regressed to the following equation, which describes the uptake of sorbate into quasi-spherical crystallites of uniform size under isobaric conditions[33]

$$\frac{N_t}{N_\infty} = 1 - \frac{6}{\pi^2}\sum_{n=1}^{\infty}\frac{1}{n^2}\exp\left(-\frac{D}{R^2}n^2\pi^2 t\right) \quad (1)$$

where $N_t$ is the molar uptake at time $t$ and $N_\infty$ is the molar uptake at equilibrium, $D$ is the effective diffusion constant of 22DMB at 353 K, and $R$ is the sphere radius.

**2.4. Reaction Testing.** Methanol conversion over H-form catalysts was carried out in a 1/4 in. stainless steel tube installed in a Thermo Scientific Lindberg Blue M furnace. The catalyst bed was supported between two plugs of quartz wool, and a K-type thermocouple (Omega Engineering) was inserted into the stainless tube to measure the temperature of the catalyst bed. Prior to the reaction, the catalyst bed was pretreated in situ at 550 °C for 3 h under flow of dried air (6 $cm^3$/min of $O_2$, 24 $cm^3$/min of $N_2$). After this pretreatment, the catalyst bed was cooled down to the reaction temperature, i.e., 350 °C. Methanol was fed by a syringe pump (Harvard Apparatus) at 7 $\mu$L/min into a heated inert gas stream of Ar (30 $cm^3$/min), which resulted in a reactant flow with a weight hourly space velocity (WHSV) of 9 $h^{-1}$. To kinetically compare the deactivation rate of the catalysts, reactions were also performed at low methanol conversions (<60%).[34] A higher space velocity was achieved by reducing the catalyst/diluent ratio while maintaining constant reactant flow rate, and data of the effluent was collected once the catalyst bed was in contact with methanol for 20 min. Reaction effluent was evaluated using an on-stream gas chromatograph (Agilent 7890B) equipped with a FID detector and an Agilent DB-1 capillary column. Methanol and dimethyl ether (DME) are considered as reactant with conversion ($X$) defined as

$$X = [1 - C_{eff}/C_{feed}] \times 100\% \quad (2)$$

where $C_{eff}$ is the carbon-based molar concentration of both methanol and DME in the effluent and $C_{feed}$ is the concentration of methanol in the feed. The selectivity ($S_i$) of hydrocarbon product $i$ is defined as

$$S_i = [C_i/C_{t,eff}] \times 100\% \quad (3)$$



DOI: 10.1021/acscatal.8b02274
ACS Catal. 2018, 8, 11042−11053

where $C_i$ is the carbon-based molar concentration of hydrocarbon $i$ in the effluent and $C_{t,eff}$ is the total carbon-based molar concentration of hydrocarbons in the effluent.

**2.5. Operando UV−Vis Microspectroscopy with Online Mass Spectrometry.** Reaction over H-form zeolite samples was performed using a Linkam cell (THMS600) equipped with a temperature controller (Linkam TMS94) and its lid was equipped with a quartz window.[35] UV−vis diffuse reflectance microspectroscopy measurements were performed with a CRAIC 20/30 PV UV−vis microspectrophotometer using a 15× objective and a 75 W xenon lamp for illumination. In a first step, the samples (~30 mg) were placed on the Linkam cell heating stage, which was further connected to cooling water. The inlet of the operando reactor setup was connected to a $N_2$ gas line, via a methanol saturator, whereas the outlet was vented. The lid of the Linkam cell was equipped with a quartz window to monitor the reaction by UV−vis diffuse reflectance microspectroscopy. The UV−vis diffuse reflectance spectra were recorded at 30 s intervals during the MTH experiment, which typically took 90 min. Prior to the MTH reaction, the samples were first heated to 400 °C at a rate of 30 °C/min and held at this temperature for 30 min in an $N_2$ atmosphere. Subsequently, the temperature was reduced to 350 °C and a constant $N_2$ flow (15 mL/min) was introduced as the carrier gas to a methanol saturator, flowing methanol to the Linkam cell. At the same time, the mass spectrometry profiles were recorded to demonstrate that the catalysts are active during the collection of UV−vis spectra. More specifically, as shown in Figure S1, the evolution of DME, methane, ethene, and propene was measured by monitoring the mass signals 45, 15, 26, and 42, respectively. At the end, the MTH reaction was quenched by rapid cooling of the Linkam cell using the same temperature controller.

## 3. RESULTS AND DISCUSSION

**3.1. Effects of Zeolite Topology.** Samples MEL-300 (ZSM-11) and MFI-300 (ZSM-5) were prepared with identical sizes of ca. 300 nm according to the synthesis conditions listed in Table 1. MEL-300 (Figure 2A) exhibits a tetragonal rod-like shape that is consistent with the morphology of ZSM-11 reported in the literature.[36] MFI-300 (Figure 2B) exhibits a disk-like morphology that is common for small ZSM-5 crystals,[37−39] whereas larger crystals tend to exhibit a hexagonal shape (as illustrated in Figure 1B). Samples of each catalyst exhibit discernible facets and a relatively monodisperse crystal size. The internal diffusion path length is defined as the distance of the identical [100] or [010] straight channels in MEL-300 and the average distance of straight [010] and sinusoidal [100] channels in MFI-300. Characteristic diffusion time scales ($R^2/D$, Table 2) are used as a proxy for effective internal diffusion time and are measured using a transient uptake experiment (Figure S2). Measured $R^2/D$ values indicate that diffusion of 22DMB is faster in MEL-300 than in MFI-300, despite SEM images showing similar averaged crystallite sizes between those two samples (Figure 2).

The crystal purity of each sample was validated by powder XRD. Comparisons of simulated XRD patterns with all samples after ion exchange and calcination to their H-form (Figure S3) indicate that ZSM-11 samples are comprised predominantly of MEL with a trace MFI impurity, consistent with prior literature reporting minor impurity phases in syntheses employing tetrabutylammonium as the OSDA.[40]

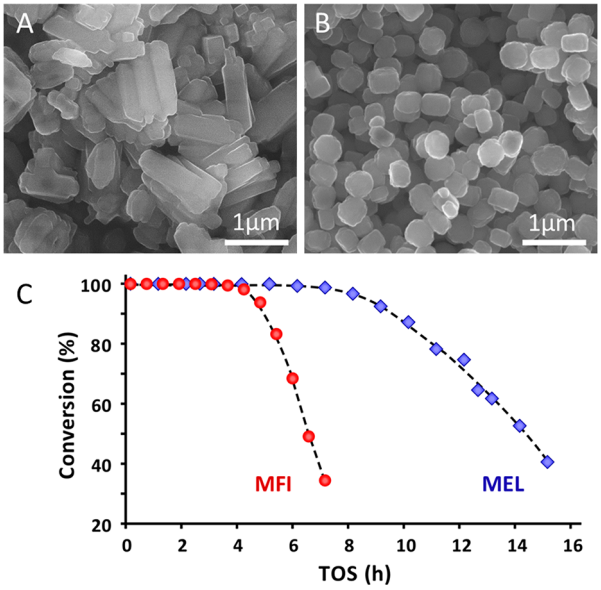


**Figure 2.** Scanning electron micrographs of samples (A) MEL-300 and (B) MFI-300. The size of MEL-300 crystals measured in the [100] dimension is 292 ± 46 nm. The size of MFI-300 crystals measured as the average of [100] and [010] dimensions is 295 ± 13 nm. Statistics are based on the measurement of at least 50 crystals. Elemental analysis (Table 2) reveals that both catalysts have similar Si/Al ratio without evidence of Al-zoning (i.e., significant differences in the spatial distribution of acid sites in the interior and exterior rim of the catalyst measured by EDS and XPS, respectively). (C) Methanol conversion as a function of TOS for H-form MEL-300 (blue diamonds) and MFI-300 (red circles) catalysts. Reactions were performed at WHSV = 9 $h^{-1}$ and 350 °C. Dashed lines are interpolations to guide the eye.

The results of textural analysis of H-form zeolites by $N_2$ adsorption, elemental analyses by EDS and XPS, and acid site density analysis by $NH_3$-TPD are provided in Table 2 where we compare the BET surface area $S_A$, micropore volume $V_{micro}$, Si/Al ratio, and acid site density for each average crystal size. All catalysts were prepared with a Si/Al ratio of 21 ± 4, and according to the comparison of EDS and XPS results, there is a relatively homogeneous distribution of Al from the bulk to the surface of the crystals. Detailed information regarding Al siting at different tetrahedral framework sites is unknown; however, we believe that the spatial distribution of acid sites is similar among all catalyst samples in this study, due in part to the nearly identical synthesis conditions and source materials used for all samples. According to the $NH_3$-TPD analysis, all catalysts show very similar acid site density with the exception of MEL-750, which has a lower value that is in line with its slightly higher Si/Al ratio. The BET surface area and micropore volume of the catalyst samples are approximately equal, regardless of crystal size and framework type. Herein, we use the series of homologous catalysts in Table 2 to elucidate structure-performance relationships in MTH wherein two properties (i.e., framework topology and crystal size) are varied, while keeping all remaining parameters fixed.

We first compare the TOS lifetime of MEL-300 and MFI-300 catalysts (Figure 2C) where a change from sinusoidal channels in MFI to straight channels in MEL has a marked impact on MTH reaction performance. Reaction conditions were selected according to a reported protocol[15] in order to achieve an initial 100% conversion of methanol. We have


DOI: 10.1021/acscatal.8b02274
ACS Catal. 2018, 8, 11042−11053

**Table 2. Characterization of ZSM-11 and ZSM-5 Catalysts**

| sample | size (nm) | BET $S_A$ ($m^2/g$) | $V_{micron}$ ($cm^3/g$) | Si/Al (EDS) | Si/Al (XPS) | $NH_3$-TPD ($\mu$mol/g) | $R^2/D$ (ks) |
|---|---|---|---|---|---|---|---|
| MEL-150 | 150 | 429 | 0.13 | 18.5 | 20.8 | 803 | 35.1 |
| MEL-300 | 300 | 434 | 0.14 | 18.0 | 24.5 | 864 | 37.7 |
| MEL-750 | 750 | 448 | 0.13 | 22.4 | 22.3 | 621 | 58.5 |
| MFI-300 | 300 | 455 | 0.14 | 18.2 | 21.2 | 782 | 49.8 |

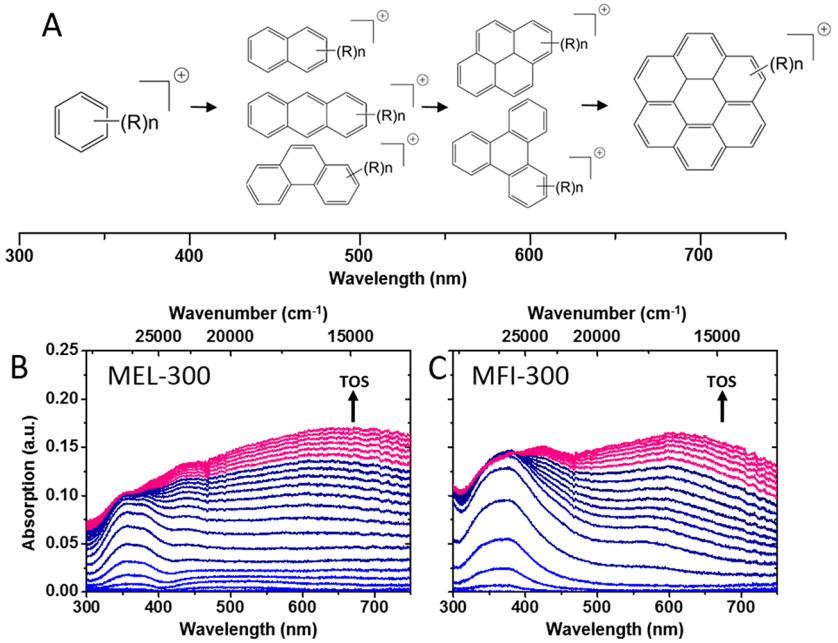


**Figure 3.** (A) Proposed coke species/precursors forming during the MTH reaction (based on a prior study of ZSM-5).[43] Operando UV−vis diffuse reflectance spectra during MTH over H-form (B) MEL-300 and (C) MFI-300 catalysts at 350 °C for TOS = 0−10 min (from blue to purple), reported in time intervals of 30 s. Measurements of both catalysts at longer times are provided in Figure S5.

observed an approximate 2-fold difference in the lifetime (i.e., methanol conversion ≥95%) between ZSM-11 and ZSM-5 (8.5 and 4.5 h, respectively). The slope of the deactivation curves for the two samples also indicates that MEL-300 deactivates more slowly after methanol breakthrough, most likely as a result of the less tortuous straight micropore channels that better facilitate intracrystalline diffusion of hydrocarbons (a more detailed analysis is provided in Section 3.2). This result qualitatively agrees with the findings of Olsbye and co-workers[15] but is opposite the trend recently reported by Wang et al.[22] who examined more siliceous ZSM-5 and ZSM-11 catalysts (Si/Al = 60−240) and claim the former exhibits a longer lifetime. Their findings are rationalized on the basis of Al occupying different tetrahedral sites in ZSM-5 (channel intersections) compared to ZSM-11 (straight channels), which suggests that Al siting impacts catalyst behavior (particularly for catalysts with low acid site density, as are those employed in their study).

To further clarify the differences in reaction behaviors between MEL-300 and MFI-300, operando UV−vis diffuse reflectance microspectroscopy was employed to measure the evolution of reaction intermediates (Figure 3A) of HCP-type species and coke precursors at the transient initial period of the reaction. In order to ensure that we have obtained relevant spectroscopic data, we are working under operando conditions; we have measured online mass spectra, indicating that the spectroscopic-reaction cell used indeed allows catalytic measurements (Figure S1). As shown in Figure 3, we observe within the first 10 min of reaction the appearance of methyl-substituted benzene cations at around 385 nm and larger aromatics (>450 nm), including naphthalenes and anthracenes.[35,41−45] Time-resolved absorption spectra for MEL-300 (Figure 3B) and MFI-300 (Figure 3C) show different evolutionary behavior of HCP species during the initial transient stage of MTH reactions. The formation of large aromatics over ZSM-11 catalysts is more rapid, as indicated by the early appearance of absorption bands above 450 nm, compared to the HCP species at 385 nm; however, for ZSM-5, there is a more gradual appearance of large aromatics relative to HCP species.

The first spectra with visible absorption bands (Figure S4B) were examined for both catalysts to study the earliest HCP species formed during the reaction. Absorption bands around 385 and 475 nm were observed for MEL-300, demonstrating that the HCP species and large aromatics formed almost simultaneously. Conversely, only one band at around 385 nm was initially observed in MFI-300, with the production of large aromatics occurring after 1 min (Figure S4A). The slightly delayed formation of large aromatic species over MFI-300 compared to that over MEL-300 (Figure S4B) could be attributed to the tortuous sinusoidal channels in the former, which hinder the diffusion of HCP species. The more rapid formation of aromatics in ZSM-11 could also be explained by its slightly larger channels and channel intersections (Figure 1) that can accommodate bulkier hydrocarbons. During the initial stage of the reaction, the aromatic hydrocarbon pool is not fully developed and most of the Brønsted acid sites are probably occupied by adsorbed methanol; aromatic molecules with high mobility (e.g., in a straight channel) should efficiently


DOI: 10.1021/acscatal.8b02274
ACS Catal. 2018, 8, 11042−11053

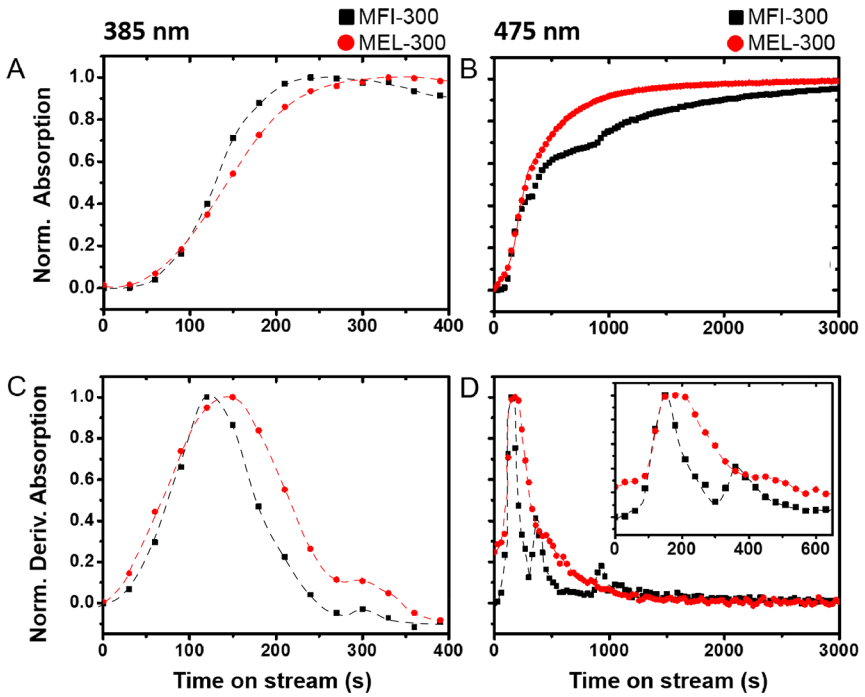


**Figure 4.** Time on stream development of the normalized Gaussian bands of methyl-substituted benzene cations at (A) 385 nm and larger aromatic species at (B) 475 nm from deconvoluted UV−vis spectra during MTH reaction over H-form MEL-300 (red circles) and MFI-300 (black squares) catalysts. The first derivative of absorbance spectra is provided in (C) for 385 nm and in (D) for 475 nm. Dashed lines are interpolations to guide the eye. Further details of spectra deconvolution are provided in the Supporting Information.

react with multiple surface-adsorbed methoxy groups or methanol to form larger, conjugated aromatic species. After 10 min of TOS, the absorption bands around 385 nm and above 450 nm exhibit little change, which is attributed to an increase in the overall baseline of absorption spectra due to the darkening of the catalysts during MTH reactions (Figure S5).[11]

Deconvolution of the time-resolved spectra was performed using Gaussian fitting with a home-made script (Figure S6) to monitor the separate peak contributions in the UV-vis data. All deconvolutions were performed in energy space, wavenumbers (Figure S6) but herein, we refer to bands in units of wavelength as this is most commonly used in literature. For comparative purposes, we selected the two most prominent absorption bands at 385 and 475 nm to represent the HCP and coke precursor species, respectively. To reduce the effect of overall darkening, i.e., the increase of the spectral baseline with TOS, the intensity of each spectrum was normalized with respect to its maximum absorption to focus on the kinetics of hydrocarbon accumulation. As shown in Figure 4, MFI-300 and MEL-300 exhibit different trends in the evolution of HCP species at 385 nm and polyarene coking species at 475 nm. A slightly longer time is required for MEL-300 to reach the maximum absorption for HCP species but much shorter time for larger aromatic species, thus demonstrating the influence of framework topology on reaction behavior. Specifically, ZSM-5 crystals are more diffusion limited than ZSM-11,[46] which facilitates the entrapment of HCP species in MFI-300. Conversely, larger aromatics form more readily in MEL-300 (Figure 4B) owing to its straight channels and slightly larger channel intersections that facilitate more rapid formation of larger HCP species compared to MFI-300.

The normalized first derivatives of the UV−vis data at 385 nm (Figure 4C) and 475 nm (Figure 4D) highlight the rates of HCP species and larger aromatics accumulation, respectively. As shown in Figure 4C, HCP species accumulate rapidly in MFI-300, with a maximum absorbance reached in a shorter time than MEL-300. We attribute this to the diffusion limitations imposed by tortuous sinusoidal channels in the MFI framework wherein hydrocarbons are more likely to be entrapped, whereas the straight channels of MEL facilitate faster diffusion of HCP species, allowing them to escape the crystals before secondary reactions lead to their entrapment. Analysis of larger aromatics in Figure 4D reveals the presence of multiple peaks. It is not possible to spatially resolve aromatic accumulation from these spectra; however, we can speculate their assignments. For instance, Weckhuysen and co-workers previously reported[45] time-resolved UV−vis microspectroscopic studies with polarized light for MTH reactions over large ZSM-5 crystals and indicated that the majority of large coke species in the range of 450−600 nm are occluded in straight channels; therefore, the first peak is most likely associated with polyaromatics formation in the straight channels. We observe shoulders in these peaks at later times (Figure 4D, inset), with MFI-300 having a slightly more pronounced secondary peak. We speculate that this peak is associated with channel intersections, which is common to both catalysts. At later times (ca. 900 s), there is a third peak observed only for MFI-300, which may correspond to polyaromatic accumulation in the sinusoidal channels, which is a structural feature that is unique to MFI.

**3.2. Effect of ZSM-11 Crystal Size.** In the previous section, we demonstrated that subtle differences in crystal topology is one factor that impacts HCP and coke precursor speciation. In this section, we work solely with ZSM-11 catalysts and probe similar aspects of mass transport limitations but shift the focus to the effects of crystal size. To this end, we prepared ZSM-11 crystals of varying size by altering the water content of the synthesis mixture (see Table 1). Dilute solutions lead to



DOI: 10.1021/acscatal.8b02274
ACS Catal. 2018, 8, 11042−11053

fewer nuclei that ultimately increase the average crystal size (sample MEL-750). Conversely, a more concentrated synthesis mixture promotes nucleation, leading to a nearly 2-fold reduction in crystal size (sample MEL-150). Scanning electron micrographs reveal that MEL-150 (Figure 5A) and MEL-750 (Figure 5B) exhibit tetragonal rod-like shapes, consistent with the typical ZSM-11 morphology illustrated in Figure 1A. In Figure 5C, we compare the TOS lifetime of ZSM-11 catalysts with different average crystal sizes. General trends in catalyst deactivation (i.e., the decrease in methanol conversion with increasing TOS) are similar for all three samples. The largest catalyst, MEL-750, resulted in the earliest methanol breakthrough at TOS ≈ 2 h, followed by MEL-300 around 6 h. The smallest catalyst, MEL-150, significantly outperformed the other two, showing no signs of deactivation until ca. 14 h. Comparison of the rate of deactivation (i.e., slope of conversion vs TOS curves) reveals a trend of decreasing rate with reduced catalyst size. In these studies, the pore topology and composition of ZSM-11 catalysts are fixed, with no significant sign of aluminum zoning as evidenced by the similar Si/Al ratio obtained from EDS and XPS (Table 2). This allows for direct comparison of MTH performance as a function of only crystal size.

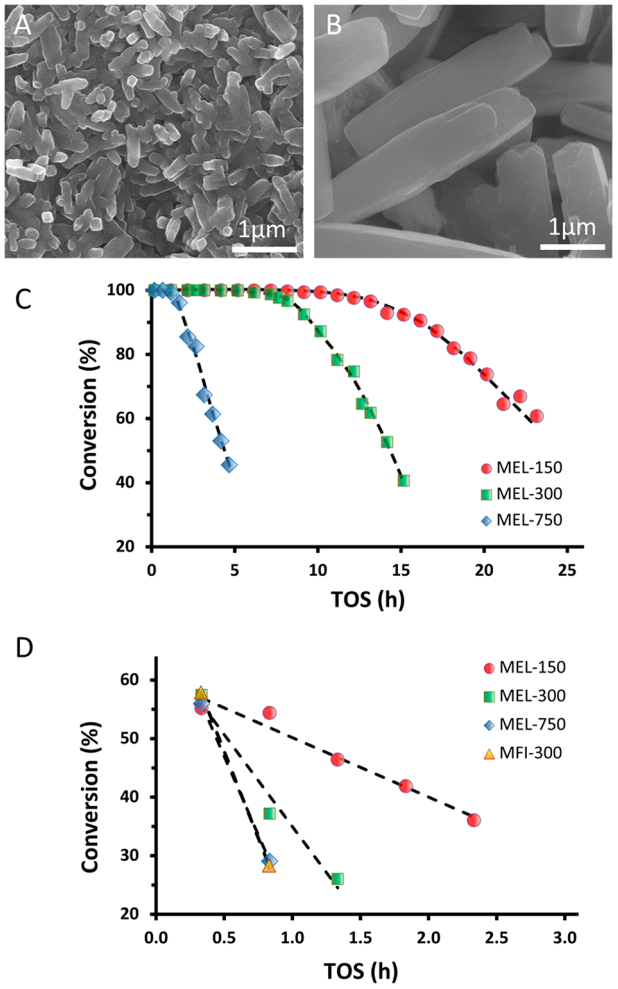


**Figure 5.** Scanning electron micrographs of samples (A) MEL-150 and (B) MEL-750. The average sizes of crystals in the [100] dimension (based on measurements of at least 50 crystals) are 152 ± 25 and 749 ± 106 nm, respectively. (C) Catalytic performance at 100% methanol conversion (*y*-axis) as a function of time on stream (*x*-axis) with WHSV = 9 $h^{-1}$. (D) Deactivation rates evaluated at low methanol conversion (*y*-axis) as a function of time on stream (*x*-axis) with variable WHSV (Table S1). All MTH reaction tests are performed at 350 °C. Comparisons are made for four catalysts: MEL-150 (red circles), MEL-300 (green squares), MEL-750 (blue diamonds), and MFI-300 (yellow triangles). Dashed lines are interpolations to guide the eye.

Lifetime is a rather nebulous parameter that is dependent upon contact time. Studies in literature often compare catalysts under similar conditions by holding space velocity and catalyst bed length fixed. Here, we use a similar approach to generate self-consistent data; however, comparisons to a broader set of results in literature must be done with caution to ensure that catalyst testing was performed under similar conditions. In our study, we define lifetime as the period of methanol conversion ≥95%. To this end, we observed an 8-fold increase in ZSM-11 lifetime (from 1.7 to 13.5 h) when the average crystal size was reduced from 750 to 150 nm. Prior studies by Ryoo and co-workers[30] used MTH as a benchmark reaction to compare commercial ZSM-5 of unspecified submicron size with 2-dimensional nanosheets (ca. 2 nm) and showed an increase in lifetime from approximately 4 to 15 days with decreasing catalyst size. This finding is qualitatively consistent with prior literature[25] reporting a general correlation between reduced crystal size and improved catalyst lifetime. Interestingly, ZSM-11 catalysts tested here exhibit a substantially higher net increase in lifetime. On the basis of our studies and those of Ryoo et al., it is reasonable to suggest that future advances in the synthesis of ZSM-11 to reduce crystal size below 100 nm have the potential to further improve MTH catalyst lifetime (beyond values reported here). To our knowledge, MEL-150 is the smallest ZSM-11 sample reported in literature as isolated (nonaggregated) crystals with well-defined facets, which is beneficial for the facile quantification of diffusion path length.

Molecular transport in zeolite channels is more restricted with increasing crystal size owing to longer diffusion path length, which was confirmed by $R^2/D$ measurements (Table 2) showing a monotonic reduction in mass transport limitations with decreasing ZSM-11 crystal size. There also exists a nearly linear correlation between the characteristic diffusion rate $D/R^2$ and catalyst lifetime, as shown in Figure S2E. Estimates of catalyst lifetime from data in Figures 2C and 5C were also compared to catalyst deactivation under subcomplete methanol conversion. The importance of evaluating catalyst lifetime from iso-conversion data has been stressed in recent editorial articles.[34,47] To this end, we compared catalyst deactivation at a starting point of ca. 55% methanol conversion. The deactivation profiles and corresponding rates of deactivation ($S_{55\%}$) under these conditions for all four ZSM-5 and ZSM-11 samples are provided in Figure 5D and Table 3, respectively. For comparison, we also report the deactivation rates of 100% conversion data ($S_{100\%}$) during the time period of catalyst deactivation, the time for methanol breakthrough ($t_{95\%}$), and the turnover number (TON). These data are tabulated in Table 3 along with their corresponding normalized (norm) values using MEL-750 as a reference.

The trends in ZSM-11 catalyst stability fall in the order of MEL-150 > MEL-300 > MEL-750 and are consistent for all metrics reported in Table 3; however, there are discrepancies for the MFI-300 sample wherein $S_{55\%}$ and $S_{100\%}$ indicate faster rates of deactivation compared to MEL-750, while $t_{95\%}$ suggests MFI-300 has a longer catalyst lifetime. The site normalized reaction rate, TON, can be used as an alternative metric to compare the deactivation rate, for which we have computed for


DOI: 10.1021/acscatal.8b02274
ACS Catal. 2018, 8, 11042−11053

**Table 3. Deactivation of ZSM-5 and ZSM-11 Catalysts**

| sample | $\lvert S_{55\%}\rvert$ ($h^{-1}$)[a] | norm $S_{55\%}$[e] | $\lvert S_{100\%}\rvert$ ($h^{-1}$)[b] | norm $S_{100\%}$[e] | $t_{95\%}$ (h)[c] | norm $t_{95\%}$[e] | $TON_{80-60\%}$[d] | norm TON[e] |
|---|---|---|---|---|---|---|---|---|
| MEL-150 | 10.2 | 0.19 | 4.3 | 0.23 | 13.5 | 7.5 | 1139 | 3.4 |
| MEL-300 | 31.4 | 0.58 | 9.0 | 0.48 | 8.5 | 4.7 | 506 | 1.5 |
| MEL-750 | 53.8 | 1.00 | 18.9 | 1.00 | 1.8 | 1.0 | 335 | 1.0 |
| MFI-300 | 59.1 | 1.10 | 29.3 | 1.55 | 4.5 | 2.5 | 172 | 0.5 |

[a]Slope of data in Figure 5D. [b]Slope of data in Figures 2C and 5C (evaluated between 80% and 50% methanol conversion). [c]Times corresponding to 95% methanol conversion in Figures 2C and 5C. [d]Turnover number (TON) obtained from the integrated area of the curves in Figures 2C and 5C using eq 4 (in units of mol converted MeOH per mol $H^+$). [e]Normalized ("norm") values relative to sample MEL-750.

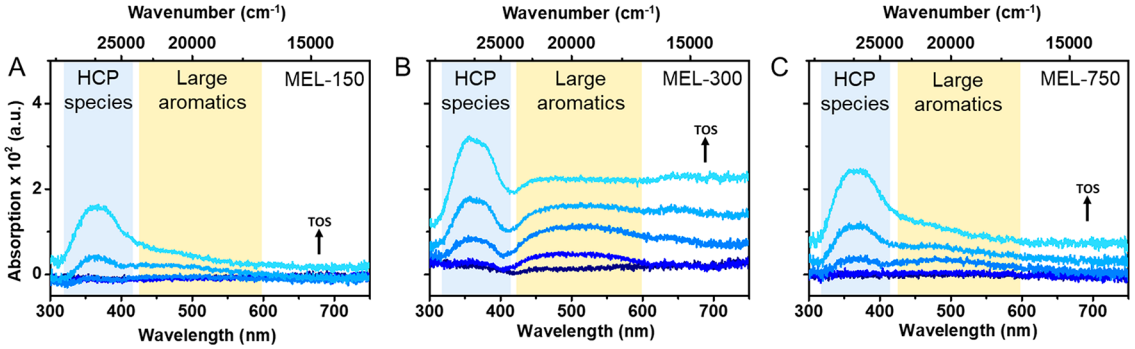


**Figure 6.** Operando UV−vis spectra from 0 to 2 min over H-form (A) MEL-150, (B) MEL-300, and (C) MEL-750 catalysts during transient conversion of methanol to hydrocarbon products. The shaded regions show HCP species and large aromatic absorption for three catalysts. Lines are colored from dark to light blue with increasing TOS.

a selected span of time on stream using a modified form of the equation reported by Bhan and co-workers,[48]

$$\mathrm{TON}(t) = \frac{1}{[\mathrm{H}^+]_0}\int_{t_1}^{t_2} F(\tau)\,\mathrm{d}\tau \tag{4}$$

where $[H^+]_0$ is the total number of Brønsted acid sites (obtained from the $NH_3$-TPD data in Table 2), $F(\tau)$ is the molar flow rate of converted carbon (reacted methanol), and $t$ is TOS selected between times $t_1$ and $t_2$ corresponding to 80% and 60% methanol conversion (i.e., regions of nearly linear deactivation in Figures 2C and 5C). The TON values show that MFI-300 deactivates twice as rapidly as MEL-750, whereas the most optimal catalyst (MEL-150) deactivates with a rate that is 3.4-times less than MEL-750. Comparison of all metrics in Table 3 reveals significant differences in the deactivation rate of each catalyst. For instance, the values of $S_{55\%}$ are much higher than $S_{100\%}$, which is consistent with an accelerated deactivation of ZSM-5 catalysts reported by Olsbye and co-workers[49] under iso-conversion conditions (i.e., higher WHSV); however, the normalized rates of deactivation for each catalyst (norm $S_{55\%}$ and norm $S_{100\%}$) are semiquantitative. Collectively, normalized data for MEL-150 catalyst stability estimate factors of 7.5, 4.3, 5.3, and 3.4 relative to MEL-750 based on $t_{95\%}$, $S_{100\%}$, $S_{55\%}$, and TON, respectively. Such variability is not unexpected but does highlight the importance of using proper (and multiple) methods of evaluating catalyst deactivation in MTH reactions.

In order to compare the influence of diffusion path length on HCP species formation before significant coking occurred, we examined the first detectable UV−vis spectra of all samples (i.e., first 2 min of reaction). Detailed analysis (Figure 6) reveals the presence of both HCP and large aromatic species in the first detectable spectra of all the three ZSM-11 catalysts, which is consistent with our claim that the simultaneous appearance of these two bands occurs in straight channels. Interestingly, spectra at early time on stream (Figure S4B) reveal an absorption ratio of large aromatics to HCP species that increases in the order of MEL-150 < MEL-750 < MEL-300. This trend continues in the first 2 min (Figure 6). The residence time of HCP species in the smallest catalyst (MEL-150) provides less opportunity for secondary reactions to larger aromatic species prior to diffusing out of the channels. This can explain why MEL-300 produces a higher percentage of large aromatics than MEL-150; however, the fact that MEL-750 yields an intermediate percentage of large aromatics cannot be rationalized by the same argument.

To explain the trend in Figure 6, we turn to traditional reaction engineering methods of identifying and comparing diffusion and reaction limited regimes. Tsapatsis and co-workers[50] invoked a similar rationale to describe the effects of ZSM-5 crystal size on catalytic performance. Notably, it can be argued that ZSM-11 catalysts with moderate Thiele modulus and effectiveness factor (Figure S8) provide sufficient residence time for secondary reactions that convert HCP species to larger aromatics. As the size of the catalyst increases and correspondingly the residence time is longer, there is a higher probability that cracking reactions reduce the size of HCP species. This most likely occurs within the interior of the catalyst where methanol concentration is less at early TOS and the number of unoccupied Brønsted acid sites is the highest. This could explain why large aromatics are less prevalent in MEL-750 compared to MEL-300. Larger catalysts are more likely to contain regions of free acid sites to crack larger HCP species, particularly at short contact times with the methanol feed. It is important to note that the conditions tested in UV−vis experiments are transient periods corresponding to the early times when methanol is first introduced into the packed bed reactor. Product distributions at later times naturally shift as HCP speciation evolves and coke progressively accumulates.

A comparison of the time to reach maximum adsorption at 385 nm (Figure 7C) and 475 nm (Figure 7D) for the three



DOI: 10.1021/acscatal.8b02274
ACS Catal. 2018, 8, 11042−11053

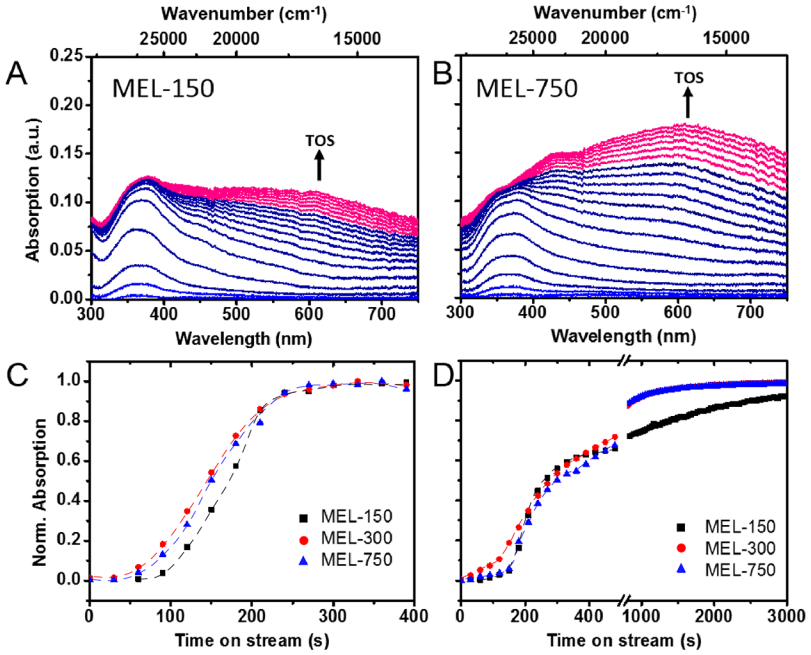


**Figure 7.** Operando UV−vis diffuse reflectance spectra during MTH reaction over H-form (A) MEL-150 and (B) MEL-750 catalysts at 350 °C for TOS = 0−10 min with time intervals of 30 s. Measurements of both catalysts at longer times are provided in Figure S7. The temporal changes in normalized Gaussian bands of methyl-substituted benzene cations at (C) 385 nm and larger aromatic species at (D) 475 nm are reported from deconvoluted UV−vis spectra during MTH reaction over catalysts MEL-150 (black squares), MEL-300 (red circles), and MEL-750 (blue triangles).

ZSM-11 catalysts shows the effect of crystal size on reaction behavior. For HCP species in Figure 7C, all catalysts quickly reached a maximum absorption within 4 min, revealing that the straight channels are sufficient for methanol and other precursors of HCP species to quickly access the acid sites. Similar comparisons for large aromatics (Figure 7D) show shorter times (ca. 25 min) for MEL-300 and MEL-750 to reach maximum absorption, while the MEL-150 catalyst does not reach a maximum within the time frame of analysis. We posit that longer diffusion path length provides sufficient residence time for precursors to react with multiple acid sites, leading to the formation of large aromatics. Conversely, the shorter path length of MEL-150 leads to a longer time frame to reach maximum aromatics production.

**3.3. MTH Product Selectivity.** The two medium-sized zeolite frameworks selected for this study yield a broad range of MTH products that are typically categorized in the following groups: $C_1$, $C_{2=}$, $C_{3=}$, $C_{4=}$, $C_2-C_4$ alkanes, $C_{5+}$ (aliphatics), and aromatics. In order to compare product selectivity with minimum influence of coking and interconversion (i.e., secondary reactions) on the hydrocarbon products, we performed iso-conversion reactions at lower conversion (ca. 55%) as described in Section 3.2, and the selectivity data is reported at a TOS of 20 min. The product selectivities for the three ZSM-11 catalysts and one ZSM-5 catalyst are provided in Figure 8. For the purpose of comparison, we use two common descriptors:

$$R_x = S_{xylenes}/\Sigma_i S_i \quad (5)$$

$$R = S_{ethene}/S_{2MBu} \quad (6)$$

The term $R_x$ is the xylene-to-aromatics ratio where $S_{xylenes}$ is the selectivity for the sum of all xylene isomers and $S_i$ is the selectivity for each aromatic compound. The term $R$ refers to the ethene-to-2MBu ratio where $S_{ethene}$ is the selectivity of ethene and $S_{2MBu}$ is the selectivity of 2MBu (defined as the sum of 2-methylbutane and 2-methyl-2-butene). The descriptor $R_x$ indirectly assesses diffusion limitations within zeolite crystals. Due to the inherent shape selectivity of zeolite catalysts, xylenes (more specifically, *p*-xylene) can diffuse easier through medium-sized pores relative to bulkier polymethybenzenes and larger aromatics. To this end, a larger value of $R_x$ is indicative of more pronounced diffusion limitations. The value of $R$ is often used to compare the aromatic- and olefin-based cycles of the HCP mechanism.[51] In the aromatic-based cycle, active polymethybenzenes undergo a series of methylation and dealkylation reactions to produce ethene and propene.

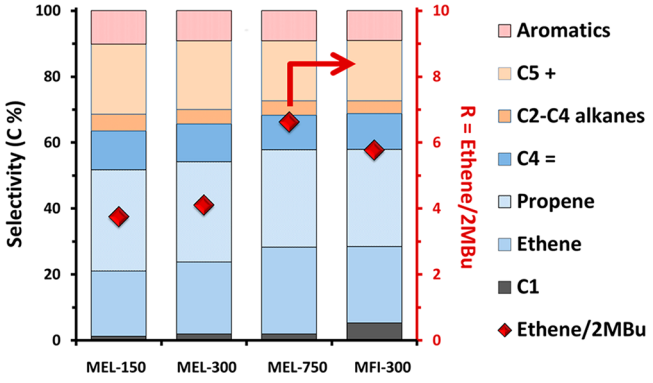


**Figure 8.** Effluent hydrocarbon selectivity (left axis) and $R$ (right axis) for MTH reactions over ZSM-11 catalysts of varying crystal size: MEL-150 (150 nm), MEL-300 (300 nm), and MEL-750 (750 nm). Comparisons are made with ZSM-5 (MFI-300, 300 nm). Detailed information is provided in Table S1. Percentages are based on the total yield of products. Reactions were performed under iso-conversion conditions (55% methanol conversion) using WHSV = 50, 50, 25, and 60 $h^{-1}$, respectively.



DOI: 10.1021/acscatal.8b02274
ACS Catal. 2018, 8, 11042−11053

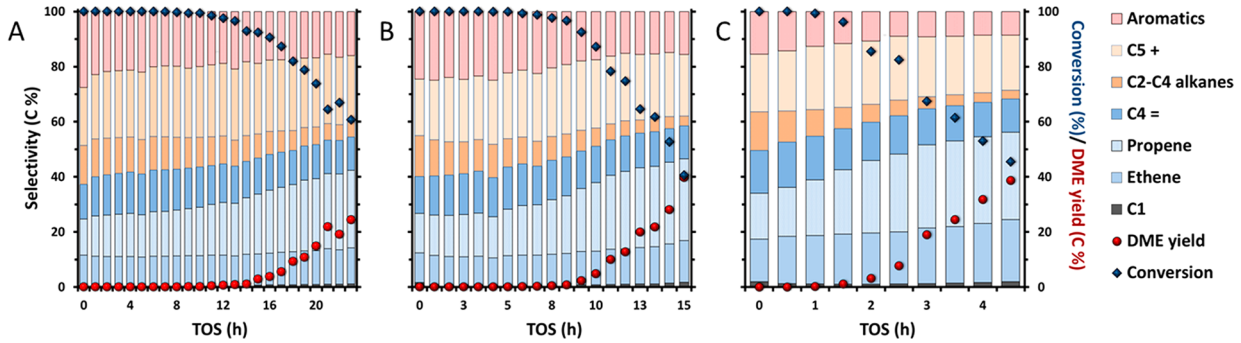


**Figure 9.** MTH product selectivity over H-form (A) MEL-150, (B) MEL-300, and (C) MEL-750 catalysts as a function of TOS. The methanol conversion (blue diamonds, taken from Figure 5C) and corresponding DME yield (red circles) are plotted to show the rate of catalyst deactivation. All reactions were performed at WHSV = 9 $h^{-1}$ and $T$ = 350 °C. The corresponding plot for MFI-300 is provided in Figure S9.

Conversely, the major products of the olefin-based cycle are propene, higher olefins, and alkanes. A higher value of $R$ is indicative of enhanced propagation of the aromatic-based cycle.[51]

Comparing all three ZSM-11 catalysts, we observe an increase in both $R$ (Figure 8) and $R_x$ (Table S1) with increasing crystal size. There is a notable increase in $R$ when the size of the catalyst is increased from MEL-150 ($R$ = 3.8) to MEL-750 ($R$ = 6.6), which reflects an enhanced aromatic-based cycle for larger zeolites. According to Khare et al.,[31] a higher Si/Al ratio results in weaker propagation of the aromatic-based cycle and lower ethene selectivity. Even though MEL-750 exhibits a slightly higher Si/Al ratio and lower acid site density compared to other catalysts in this study, it still falls in a monotonic trend of increasing $R$ with increasing crystal size. We also observe an increase in $R_x$ from 0.56 to 0.70 with increased crystal size, which is expected on the basis of faster rates of xylene diffusion relative to other bulkier aromatics with increased mass transfer resistance. Close inspection of the selectivity data in Figure 8 also reveals that all ZSM-11 catalysts have low $C_1$ selectivity (≤2%). The $C_{2=}$ selectivity increases with catalyst size, commensurate with the enhanced aromatic-based cycle. Conversely, the $C_{5+}$ (aliphatics) selectivity decreases with increasing crystal size owing to a weaker olefin-based cycle. Collectively, the trends observed for various sizes of ZSM-11 catalysts are similar to those reported by Khare et al.[24] for ZSM-5 who examined DME conversion to hydrocarbons and reported a monotonic increase in $C_2$ selectivity and decrease in $C_{4+}$ selectivity with increasing crystal size. Our findings indicate that $C_{3=}$ and aromatics selectivities are independent of crystal size. The result for $C_{3=}$ is not unexpected given that it can be produced by both catalytic cycles and is seemingly unaffected by shifts in the relative strength of each cycle. In terms of aromatics selectivity, it would be expected to increase with a stronger aromatic-based cycle; however, a larger crystal size also imposes more diffusion limitations for bulkier products, which can lower product yields, leading to two offsetting effects giving rise to a relatively constant aromatic selectivity within the ZSM-11 catalyst size range considered in this study.

Comparison of ZSM-5 and ZSM-11 in Figure 8 reveals that a 300 nm ZSM-5 catalyst would be expected to perform similarly to a 615 nm ZSM-11 catalyst (i.e., an interpolated size based on $R$ values for MEL-300 and -750). Therefore, it appears that altering the topology of zeolites from straight to sinusoidal channels has a similar effect as increasing crystal size. In other words, the limitation on molecular diffusion that is imposed by tortuous sinusoidal channels in MFI is analogous to extending the length of straight channels in MEL. Given that the product distribution profiles of ZSM-11 and ZSM-5 catalysts are comparable, we find that the subtle difference in pore topology has little impact on selectivity. A direct comparison between MEL-300 and MFI-300 (i.e., catalysts of identical size) reveals that the latter has higher $R$ and $R_x$, which is consistent with an increased aromatic-based cycle for ZSM-5, leading to more rapid coking. One notable difference between the two zeolite frameworks is a higher $C_1$ selectivity for ZSM-5. Bhan and co-workers[52] have attributed methane formation as a product of methanol disproportionation, where higher methanol partial pressure local to the active sites engenders higher methane selectivity and shorter catalyst lifetime. Here, we observe that, in order to achieve iso-conversion of ∼55%, MFI-300 requires slightly higher space velocity (WHSV = 60 $h^{-1}$) compared to MEL-300 (WHSV = 50 $h^{-1}$). The higher space velocity for MFI-300 may result in higher average methanol partial pressure throughout the catalyst bed, which is qualitatively consistent with the higher methane selectivity. This can potentially explain why catalytic runs over MFI-300, which were performed at lower space velocity (WHSV = 9 $h^{-1}$), result in methane selectivity less than 2% (Figure S9).

In Figure 9, we compare the product selectivity with time on stream for all three ZSM-11 samples at a constant WHSV = 9 $h^{-1}$ (the corresponding plot for ZSM-5 is provided in Figure S9). The selectivity is plotted along with temporal changes in conversion and the DME yield. Trends in the latter mirror the former and, thus, can be used as a surrogate for tracking catalyst deactivation. At early TOS with high methanol conversion, propene and other light olefins can be further converted to heavier aliphatic and aromatic products.[15] We observe that regardless of catalyst size, the $C_{3=}$ selectivity increases with catalyst deactivation, whereas alkane and aromatic selectivity exhibit an opposite trend. This seems to indicate that, during early TOS, when methanol is fully converted, there are ample fresh active sites downstream of the catalyst bed where the olefin products from MTH reactions upstream can form alkanes and aromatics through hydrogen transfer and cyclization. Comparing different ZSM-11 catalysts, we observe that $C_{2=}$ selectivity increases with larger crystal size, which is consistent with catalytic studies under iso-conversion conditions (Figure 8). One notable difference in studies at 55% and 100% methanol conversion is a decreasing aromatic selectivity with increasing crystal size in the latter case. We speculate that, for smaller crystal sizes, it is easier for the aromatic products to diffuse out of the crystal rather than becoming entrapped within the pores and developing into polyarene coking species. This is consistent with UV−vis data (e.g., Figure 7D) showing that a



DOI: 10.1021/acscatal.8b02274
ACS Catal. 2018, 8, 11042−11053

much longer time is required for MEL-150 to reach its maximum absorption of coking species.

## 4. CONCLUSIONS

A series of zeolite ZSM-11 and ZSM-5 catalysts with carefully controlled physicochemical properties were synthesized to study the effects of framework topology and diffusion path length on the MTH reaction. A direct comparison of ZSM-5 and ZSM-11 with nearly identical crystal size and Si/Al ratio shows that the MEL framework results in a ca. 2-fold increase in catalyst lifetime owing to its straight micropore channels that better facilitate molecular diffusion. A switch in ZSM-11 catalyst size from 750 to 150 nm resulted in an 8-fold increase in catalyst lifetime, consistent with the general trend for ZSM-5 reported in literature. Using operando UV−vis microspectroscopy, we demonstrated that crystal size and porous architecture have distinct influences on the evolution of hydrocarbon pool and coke speciation during early (transient) time on stream. Such differences lead to distinct lifetime among ZSM-11 and ZSM-5 catalysts of varying crystal size. Systematic investigation of MTH product selectivity under iso-conversion conditions reveals that more pronounced diffusion limitations (i.e., increased catalyst size) promote the aromatic-based hydrocarbon pool cycle, leading to increased $C_{2=}$ selectivity. Moreover, our findings suggest that ZSM-11 is a promising alternative to ZSM-5 for MTH catalysis and potentially other reactions where diffusion limitations leading to rapid coking sacrifice catalyst performance.

## ■ ASSOCIATED CONTENT

### Supporting Information

The Supporting Information is available free of charge on the ACS Publications website at DOI: 10.1021/acscatal.8b02274.

The mass spectra and additional operando UV−vis spectra for ZSM-11 and ZSM-5 samples during MTH reaction; 22DMB adsorption data; XRD patterns of catalysts; transient selectivity over MFI-300 catalyst; table of iso-conversion reaction results (PDF)

## ■ AUTHOR INFORMATION


### Corresponding Authors

*E-mail: jrimer@central.uh.edu.
*E-mail: b.m.weckhuysen@uu.nl.

### ORCID

Bert M. Weckhuysen: 0000-0001-5245-1426
Jeffrey D. Rimer: 0000-0002-2296-3428


### Notes

The authors declare no competing financial interest.

## ■ ACKNOWLEDGMENTS

J.D.R. acknowledges support primarily from the U.S. Department of Energy, Office of Science, Office of Basic Energy Sciences under Award Number DE-SC0014468. Additional support was provided by the Welch Foundation (Award E-1794). This work is supported by the NWO Gravitation program, Netherlands Center for Multiscale Catalytic Energy Conversion (MCEC), and a European Research Council (ERC) Advanced Grant (no. 321140). J.E.S. has received funding from the European Union's Horizon 2020 research and innovation programme under the Marie Sklodowska-Curie grant agreement No. 702149. We wish to thank Prof. Aditya Bhan and Zhichen Shi (University of Minnesota) for their help with diffusivity measurements and also for valuable discussions.

## ■ REFERENCES


(1) Chang, C. D. Hydrocarbons from Methanol. *Catal. Rev.: Sci. Eng.* **1983**, *25*, 1−118.
(2) Ilias, S.; Bhan, A. Mechanism of the Catalytic Conversion of Methanol to Hydrocarbons. *ACS Catal.* **2013**, *3*, 18−31.
(3) Tian, P.; Wei, Y.; Ye, M.; Liu, Z. Methanol to Olefins (MTO): From Fundamentals to Commercialization. *ACS Catal.* **2015**, *5*, 1922−1938.
(4) Olsbye, U.; Svelle, S.; Bjørgen, M.; Beato, P.; Janssens, T. V. W.; Joensen, F.; Bordiga, S.; Lillerud, K. P. Conversion of Methanol to Hydrocarbons: How Zeolite Cavity and Pore Size Controls Product Selectivity. *Angew. Chem., Int. Ed.* **2012**, *51*, 5810−5831.
(5) Chang, C. D. The New Zealand Gas-to-Gasoline Plant: An Engineering Tour de Force. *Catal. Today* **1992**, *13*, 103−111.
(6) Liang, J.; Li, H.; Zhao, S.; Guo, W.; Wang, R.; Ying, M. Characteristics and Performance of SAPO-34 Catalyst for Methanol-to-Olefin Conversion. *Appl. Catal.* **1990**, *64*, 31−40.
(7) Koempel, H.; Liebner, W. Lurgi's Methanol To Propylene (MTP) Report on a Successful Commercialisation. In *Studies in Surface Science and Catalysis*; Bellot Noronha, F., Schmal, M., Falabella Sousa-Aguiar, E., Eds.; Elsevier: Amsterdam, 2007; p 261−267.
(8) Olsbye, U.; Svelle, S.; Lillerud, K. P.; Wei, Z. H.; Chen, Y. Y.; Li, J. F.; Wang, J. G.; Fan, W. B. The Formation and Degradation of Active Species during Methanol Conversion over Protonated Zeotype Catalysts. *Chem. Soc. Rev.* **2015**, *44*, 7155−7176.
(9) Rojo-Gama, D.; Signorile, M.; Bonino, F.; Bordiga, S.; Olsbye, U.; Lillerud, K. P.; Beato, P.; Svelle, S. Structure−Deactivation Relationships in Zeolites during the Methanol−to-Hydrocarbons Reaction: Complementary Assessments of the Coke Content. *J. Catal.* **2017**, *351*, 33−48.
(10) Mores, D.; Stavitski, E.; Kox, M. H. F.; Kornatowski, J.; Olsbye, U.; Weckhuysen, B. M. Space- and Time-Resolved In-situ Spectroscopy on the Coke Formation in Molecular Sieves: Methanol-to-Olefin Conversion over H-ZSM-5 and H-SAPO-34. *Chem. - Eur. J.* **2008**, *14*, 11320−11327.
(11) Goetze, J.; Meirer, F.; Yarulina, I.; Gascon, J.; Kapteijn, F.; Ruiz-Martínez, J.; Weckhuysen, B. M. Insights into the Activity and Deactivation of the Methanol-to-Olefins Process over Different Small-Pore Zeolites As Studied with Operando UV−vis Spectroscopy. *ACS Catal.* **2017**, *7*, 4033−4046.
(12) Li, Z.; Navarro, M. T.; Martinez-Triguero, J.; Yu, J.; Corma, A. Synthesis of Nano-SSZ-13 and Its Application in the Reaction of Methanol to Olefins. *Catal. Sci. Technol.* **2016**, *6*, 5856−5863.
(13) Pinilla-Herrero, I.; Olsbye, U.; Márquez-Álvarez, C.; Sastre, E. Effect of Framework Topology of SAPO Catalysts on Selectivity and Deactivation Profile in the Methanol-to-Olefins Reaction. *J. Catal.* **2017**, *352*, 191−207.
(14) Molino, A.; Lukaszuk, K. A.; Rojo-Gama, D.; Lillerud, K. P.; Olsbye, U.; Bordiga, S.; Svelle, S.; Beato, P. Conversion of Methanol to Hydrocarbons over Zeolite ZSM-23 (MTT): Exceptional Effects of Particle Size on Catalyst Lifetime. *Chem. Commun.* **2017**, *53*, 6816−6819.
(15) Bleken, F.; Skistad, W.; Barbera, K.; Kustova, M.; Bordiga, S.; Beato, P.; Lillerud, K. P.; Svelle, S.; Olsbye, U. Conversion of Methanol over 10-Ring Zeolites with Differing Volumes at Channel Intersections: Comparison of TNU-9, IM-5, ZSM-11 and ZSM-5. *Phys. Chem. Chem. Phys.* **2011**, *13*, 2539−2549.
(16) Bhawe, Y.; Moliner-Marin, M.; Lunn, J. D.; Liu, Y.; Malek, A.; Davis, M. Effect of Cage Size on the Selective Conversion of Methanol to Light Olefins. *ACS Catal.* **2012**, *2*, 2490−2495.
(17) Teketel, S.; Svelle, S.; Lillerud, K.-P.; Olsbye, U. Shape-Selective Conversion of Methanol to Hydrocarbons Over 10-Ring Unidirectional-Channel Acidic H-ZSM-22. *ChemCatChem* **2009**, *1*, 78−81.
(18) Jacobs, P. A.; Martens, J. A. In *Synthesis of High-Silica Aluminosilicate Zeolites*; Elsevier: Amsterdam, 1987; p 167−176.




DOI: 10.1021/acscatal.8b02274
*ACS Catal.* 2018, 8, 11042−11053

(19) Zhang, C.-L.; Li, S.; Yuan, Y.; Zhang, W.-X.; Wu, T.-H.; Lin, L.-W. Aromatization of Methane in the Absence of Oxygen over Mo-based Catalysts Supported on Different Types of Zeolites. *Catal. Lett.* **1998**, *56*, 207−213.
(20) Zhang, L.; Liu, H.; Li, X.; Xie, S.; Wang, Y.; Xin, W.; Liu, S.; Xu, L. Differences Between ZSM-5 and ZSM-11 Zeolite Catalysts in 1-Hexene Aromatization and Isomerization. *Fuel Process. Technol.* **2010**, *91*, 449−455.
(21) Kustova, M. Y.; Rasmussen, S. B.; Kustov, A. L.; Christensen, C. H. Direct NO Decomposition over Conventional and Mesoporous Cu-ZSM-5 and Cu-ZSM-11 Catalysts: Improved Performance with Hierarchical Zeolites. *Appl. Catal., B* **2006**, *67*, 60−67.
(22) Wang, S.; Wang, P.; Qin, Z.; Chen, Y.; Dong, M.; Li, J.; Zhang, K.; Liu, P.; Wang, J.; Fan, W. Relation of Catalytic Performance to the Aluminum Siting of Acidic Zeolites in the Conversion of Methanol to Olefins, Viewed via a Comparison between ZSM-5 and ZSM-11. *ACS Catal.* **2018**, *8*, 5485−5505.
(23) Derouane, E. G.; Dejaifve, P.; Gabelica, Z.; Vedrine, J. C. Molecular Shape Selectivity of ZSM-5, Modified ZSM-5 and ZSM-11 Type Zeolites. *Faraday Discuss. Chem. Soc.* **1981**, *72*, 331−344.
(24) Khare, R.; Millar, D.; Bhan, A. A Mechanistic Basis for the Effects of Crystallite Size on Light Olefin Selectivity in Methanol-to-Hydrocarbons Conversion on MFI. *J. Catal.* **2015**, *321*, 23−31.
(25) Jang, H.-G.; Min, H.-K.; Lee, J. K.; Hong, S. B.; Seo, G. SAPO-34 and ZSM-5 Nanocrystals' Size Effects on Their Catalysis of Methanol-to-Olefin Reactions. *Appl. Catal., A* **2012**, *437*−*438*, 120−130.
(26) Chen, D.; Moljord, K.; Fuglerud, T.; Holmen, A. The Effect of Crystal Size of SAPO-34 on the Selectivity and Deactivation of the MTO Reaction. *Microporous Mesoporous Mater.* **1999**, *29*, 191−203.
(27) Hereijgers, B. P. C.; Bleken, F.; Nilsen, M. H.; Svelle, S.; Lillerud, K.-P.; Bjørgen, M.; Weckhuysen, B. M.; Olsbye, U. Product Shape Selectivity Dominates the Methanol-to-Olefins (MTO) Reaction over H-SAPO-34 Catalysts. *J. Catal.* **2009**, *264*, 77−87.
(28) Dai, W.; Wu, G.; Li, L.; Guan, N.; Hunger, M. Mechanisms of the Deactivation of SAPO-34 Materials with Different Crystal Sizes Applied as MTO Catalysts. *ACS Catal.* **2013**, *3*, 588−596.
(29) Auroux, A.; Dexpert, H.; Leclercq, C.; Vedrine, J. Chemical, Physical and Catalytic Properties of ZSM-5 and ZSM-11 Zeolites: a Study by Electron Microscopy, EDX-STEM and XPS. *Appl. Catal.* **1983**, *6*, 95−119.
(30) Choi, M.; Na, K.; Kim, J.; Sakamoto, Y.; Terasaki, O.; Ryoo, R. Stable Single-Unit-Cell Nanosheets of Zeolite MFI as Active and Long-Lived Catalysts. *Nature* **2009**, *461*, 246−249.
(31) Khare, R.; Liu, Z.; Han, Y.; Bhan, A. A Mechanistic Basis for the Effect of Aluminum Content on Ethene Selectivity in Methanol-to-Hydrocarbons Conversion on HZSM-5. *J. Catal.* **2017**, *348*, 300−305.
(32) *IZA Structure Commission*. Available from: http://www.iza-structure.org/.
(33) Crank, J. *The Mathematics of Diffusion*; Clarendon Press: Oxford, 1975; p 414.
(34) Scott, S. L. A Matter of Life(time) and Death. *ACS Catal.* **2018**, *8*, 8597−8599.
(35) Fu, D.; Schmidt, J. E.; Ristanović, Z.; Chowdhury, A. D.; Meirer, F.; Weckhuysen, B. M. Highly Oriented Growth of Catalytically Active Zeolite ZSM-5 Films with a Broad Range of Si/Al Ratios. *Angew. Chem., Int. Ed.* **2017**, *56*, 11217−11221.
(36) Terasaki, O.; Ohsuna, T.; Sakuma, H.; Watanabe, D.; Nakagawa, Y.; Medrud, R. C. Direct Observation of "Pure MEL Type" Zeolite. *Chem. Mater.* **1996**, *8*, 463−468.
(37) Lupulescu, A. I.; Rimer, J. D. Tailoring Silicalite-1 Crystal Morphology with Molecular Modifiers. *Angew. Chem., Int. Ed.* **2012**, *51*, 3345−3349.
(38) Chawla, A.; Li, R.; Jain, R.; Clark, R. J.; Sutjianto, J. G.; Palmer, J. C.; Rimer, J. D. Cooperative Effects of Inorganic and Organic Structure-Directing Agents in ZSM-5 Crystallization. *Molecular Systems Design & Engineering* **2018**, *3*, 159−170.
(39) Zhang, Q.; Chen, G.; Wang, Y.; Chen, M.; Guo, G.; Shi, J.; Luo, J.; Yu, J. High-Quality Single-Crystalline MFI-Type Nanozeolites: A Facile Synthetic Strategy and MTP Catalytic Studies. *Chem. Mater.* **2018**, *30*, 2750−2758.
(40) Piccione, P. M.; Davis, M. E. A new Structure-Directing Agent for the Synthesis of Pure-Phase ZSM-11. *Microporous Mesoporous Mater.* **2001**, *49*, 163−169.
(41) Vogt, C.; Weckhuysen, B. M.; Ruiz-Martínez, J. Effect of Feedstock and Catalyst Impurities on the Methanol-to-Olefin Reaction over H-SAPO-34. *ChemCatChem* **2017**, *9*, 183−194.
(42) Palumbo, L.; Bonino, F.; Beato, P.; Bjørgen, M.; Zecchina, A.; Bordiga, S. Conversion of Methanol to Hydrocarbons: Spectroscopic Characterization of Carbonaceous Species Formed over H-ZSM-5. *J. Phys. Chem. C* **2008**, *112*, 9710−9716.
(43) Nordvang, E. C.; Borodina, E.; Ruiz-Martínez, J.; Fehrmann, R.; Weckhuysen, B. M. Effects of Coke Deposits on the Catalytic Performance of Large Zeolite H-ZSM-5 Crystals during Alcohol-to-Hydrocarbon Reactions as Investigated by a Combination of Optical Spectroscopy and Microscopy. *Chem. - Eur. J.* **2015**, *21*, 17324−17335.
(44) Bjorgen, M.; Bonino, F.; Kolboe, S.; Lillerud, K. P.; Zecchina, A.; Bordiga, S. Spectroscopic Evidence for a Persistent Benzenium Cation in Zeolite H-Beta. *J. Am. Chem. Soc.* **2003**, *125*, 15863−15868.
(45) Mores, D.; Kornatowski, J.; Olsbye, U.; Weckhuysen, B. M. Coke Formation during the Methanol-to-Olefin Conversion: In Situ Microspectroscopy on Individual H-ZSM-5 Crystals with Different Brønsted Acidity. *Chem. - Eur. J.* **2011**, *17*, 2874−2884.
(46) Shen, D.; Rees, L. V. C. Frequency Response Technique Measurements of p-Xylene Diffusion in Silicalite-1 and −2. *J. Chem. Soc., Faraday Trans.* **1993**, *89*, 1063−1065.
(47) Schüth, F.; Ward, M. D.; Buriak, J. M. Common Pitfalls of Catalysis Manuscripts Submitted to Chemistry of Materials. *Chem. Mater.* **2018**, *30*, 3599−3600.
(48) Hwang, A.; Prieto-Centurion, D.; Bhan, A. Isotopic Tracer Studies of Methanol-to-Olefins Conversion over HSAPO-34: The Role of the Olefins-based Catalytic Cycle. *J. Catal.* **2016**, *337*, 52−56.
(49) Bleken, F. L.; Janssens, T. V. W.; Svelle, S.; Olsbye, U. Product Yield in Methanol Conversion over ZSM-5 is Predominantly Independent of Coke Content. *Microporous Mesoporous Mater.* **2012**, *164*, 190−198.
(50) Zhang, X.; Liu, D.; Xu, D.; Asahina, S.; Cychosz, K. A.; Agrawal, K. V.; Al Wahedi, Y.; Bhan, A.; Al Hashimi, S.; Terasaki, O.; Thommes, M.; Tsapatsis, M. Synthesis of Self-Pillared Zeolite Nanosheets by Repetitive Branching. *Science* **2012**, *336*, 1684−1687.
(51) Ilias, S.; Khare, R.; Malek, A.; Bhan, A. A Descriptor for the Relative Propagation of the Aromatic- and Olefin-Based Cycles in Methanol-to-Hydrocarbons Conversion on H-ZSM-5. *J. Catal.* **2013**, *303*, 135−140.
(52) Hwang, A.; Kumar, M.; Rimer, J. D.; Bhan, A. Implications of Methanol Disproportionation on Catalyst Lifetime for Methanol-to-Olefins Conversion by HSSZ-13. *J. Catal.* **2017**, *346*, 154−160.


DOI: 10.1021/acscatal.8b02274
*ACS Catal.* 2018, 8, 11042−11053